RSC Advances

PAPER

View Article Online
View Journal | View Issue

Cite this: *RSC Adv.*, 2023, **13**, 14033

Strongly bound Wannier–Mott exciton in pristine (LaO)MnAs and origin of ferrimagnetism in F-doped (LaO)MnAs†

Jessie Manopo, [abc] Tio Prince Lubis,[ab] Muhammad Arief Mustajab Enha Maryono, [b] Pepen Arifin,[b] Toto Winata,[b] Rena Widita [d] and Yudi Darma [*abc]

We study the electronic, magnetic, and optical properties of $(LaO_{1-x}F_x)MnAs$ ($x = 0$, 0.0625, 0.125, 0.25) systems, calculated using the generalized gradient approximation (GGA) corrected by Hubbard energy (U) = 1 eV. For $x = 0$, this system shows equal bandgap (E_g) values for spin-up and spin-down of 0.826 eV, with antiferromagnetic (AFM) properties and local magnetic moment in the Mn site of 3.86 μ_B per Mn. By doping F with $x = 0.0625$, the spin-up and spin-down E_g values decrease to 0.778 and 0.798 eV, respectively. This system, along with antiferromagnetic properties, also has a local magnetic moment in the Mn site of 3.83 μ_B per Mn. Increasing doping F to $x = 0.125$ induces increases of E_g to 0.827 and 0.839 eV for spin-up and spin-down. However, the AFM remains, where μ_{Mn} slightly decreases to 3.81 μ_B per Mn. Furthermore, the excess electron from the F ion induces the Fermi level to move toward the conduction band and changes the bandgap type from indirect bandgap ($\Gamma \rightarrow M$) to direct bandgap ($\Gamma \rightarrow \Gamma$). Increasing x to 25% induces the decrease of spin-up and spin-down E_g to 0.488 and 0.465 eV, respectively. This system shows that the AFM changes to ferrimagnetism (FIM) for $x = 25\%$, with a total magnetic moment of 0.78 μ_B per cell, which is mostly contributed by Mn 3d and As 4p local magnetic moments. The change from AFM to FIM behavior results from competition between superexchange AFM ordering and Stoner's exchange ferromagnetic ordering. Pristine (LaO)MnAs exhibits high excitonic binding energy (~146.5 meV) due to a flat band structure. Our study shows that doping F in the (LaO)MnAs system significantly modifies the electronic, magnetic, and optical properties for novel advanced device applications.

Received 7th March 2023
Accepted 23rd April 2023

DOI: 10.1039/d3ra01506h

rsc.li/rsc-advances

Introduction

The layered oxypnictide (LnO)TPn (Ln = lanthanide, T = transition metal, and Pn = pnictide) has various physical properties that have attracted much attention and intensive investigations. The superconducting properties were discovered in (LaO)FeAs by doping F at high Curie temperature (26 K T_C).[1] (LnO)CoAs shows itinerant ferromagnetism with T_C between 60 K and 80 K.[2–4] LaONiAs exhibits superconducting transition at $T_C \sim 2.4$ K[5] and a strong-coupling superconducting behavior with the enhanced T_C by F substitutional doping at O sites.[6] (LaO)ZnPn (Pn = P, As, Sb) shows diamagnetic semiconductor behavior for (LaO)ZnP and paramagnetic semiconductor for (LaO)ZnAs and (LaO)ZnSb.[7–10]

(LaO)MnAs is one of the manganese-based layered oxypnictides, formed by La–O blocking layers and Mn–As layers stacked alternately along the c-axis. Arsenic ions are surrounded tetrahedrally by Mn, and La ions are surrounded by O. (LaO)MnAs exhibits negative giant magnetoresistance of up to −24% at 200 K.[11] (LaO)MnAs is an antiferromagnetic semiconductor with high Néel temperature (317 K T_N),[11,12] and the antiferromagnetic semiconductor is seen as a promising material for spintronic devices because it has a higher magnetic ordering temperature than diluted magnetic semiconductors (DMSs). This suggestion is indicated by the high temperature.[13,14] (LaO)MnAs also exhibits Mott insulator behavior[15,16] due to the superexchange interaction between Mn and As ions,[12] making this material interesting to study and develop.

[a]*Quantum Semiconductor and Devices Lab, Department of Physics, Faculty of Mathematics and Natural Sciences, Bandung Institute of Technology, Jalan Ganesha 10, Bandung, 40132, Indonesia. E-mail: yudi@itb.ac.id*

[b]*Physics of Electronic Materials Research Division, Department of Physics, Faculty of Mathematics and Natural Sciences, Bandung Institute of Technology, Jalan Ganesha 10, Bandung, 40132, Indonesia*

[c]*Research Collaboration Center for Quantum Technology 2.0, Bandung 40132, Indonesia*

[d]*Nuclear Physics and Biophysics Research Division, Department of Physics, Faculty of Mathematics and Natural Sciences, Bandung Institute of Technology, Jalan Ganesha 10, Bandung, 40132, Indonesia*

† Electronic supplementary information (ESI) available. See DOI: https://doi.org/10.1039/d3ra01506h

Experimental research has reported the indirect bandgap value (~1.4 eV) for (LaO)MnAs.[17] A theoretical study reports an indirect bandgap of 0.46 eV and a magnetic moment of 3.54 μ_B per Mn cell from calculations based on density functional theory using generalized gradient approximation (GGA).[18]

Various doping approaches have been performed to modify the properties of the (LaO)MnAs system. A study in physical properties of the (LaO)MnAs layer due to F and Zn doping in the form of polycrystals grown by solid-state reaction method showed a clear increase in the lattice constants (a and c) for F doping. Increasing doping F in (LaO)MnAs decreases the absolute value of electrical resistivity dramatically (0–300 K), with a phase change from antiferromagnetic to paramagnetic properties. However, Zn substitution does not show apparent dependence on the resistivity.[16] On the other hand, hole doping also changes the electronic properties of this system,[19] and doping holes into [LaO] layers changes the antiferromagnetic insulating to ferromagnetic metallic behavior at room temperature (RT). The doping was performed by inducing defects in [LaO] layers. Achieving $x = 0.3$, the $(LaO)_{1-x}MnAs$ system exhibits metallic behavior for $T < 150$ K.[20]

In a previous work, we investigated the electronic and magnetic properties of the (LaO)MnAs system, again using a GGA functional, with Hubbard energy (U) applied for the Mn 3d orbital of 0–10 eV. The term U is significant in changing the structural properties, E_g, and magnetic moment of the Mn ion. Our calculation shows that the E_g of the system increases with the U value, with the maximum value at $U = 8$ eV, which is the closest E_g to the experimental result[17] but shows an overestimated lattice parameter. In considering the structural properties, the value of $U = 1$ eV is the most appropriate, which leads to E_g and μ_{Mn} of 0.834 eV and 4.31 μ_B. Increasing U induces increased local-symmetry distortions in $MnAs_4$ and OLa_4.[21]

In this paper, we study the structural, electronic, magnetic, and optical properties of layered manganese-based (LaO)MnAs, with doping F^- ions at the O^{2-} site. This system was calculated by first principles based on the density functional theory (DFT). We studied $(LaO_{1-x}F_x)MnAs$, where $x = 0$, 0.0625, 0.125, and 0.25. The structural parameters are systematically reported. The electronic properties are discussed in terms of band structure, and magnetic properties are discussed in terms of density of states (DOS). Energy-dependent total and projected DOS were revealed to find the electronic properties of each orbital. Finally, the dielectric function is also calculated to reveal its optical properties, which are yet to be explored.

Computational methodology

We used the Quantum ESPRESSO code[22] to calculate the electronic and magnetic structure of $(LaO_{1-x}F_x)MnAs$. Our previous calculations using Quantum ESPRESSO confirmed accurate results supporting the experimental data.[23] In this work, our calculation accomplishes the plane-wave method within the generalized gradient approximation (GGA) and employing the Perdew–Burke–Ernzerhof (PBE)-type exchange–correlation functional energy.[24]

As the host material, (LaO)MnAs has a tetragonal crystal structure with the centrosymmetric space group $P4/nmm$. From the experimental result, we use the initial structural parameters $a = b = 4122$ Å and $c = 9048$ Å.[12] For the self-consistence-field (SCF) calculation, we set the threshold energy of 10^{-3} hartree (~2.72×10^{-3} eV), cut-off kinetic energy at 50 Rydberg (~680 eV), and k-point mesh of $8 \times 8 \times 4$ ($x = 0$) and $5 \times 5 \times 4$ ($x =$ 0.0625, 0.125, and 0.25). We use the on-site Coulomb repulsion energy (U)[25] in the Mn 3d orbital with $U = 1$ eV, which is the most appropriate value considering the structural properties.[21] For band calculation, we calculated within a k-point path of M–A–Z–Γ–X–M–Γ in the corresponding Brillouin zone, as in our previous work.[21] Non-self-consistent-field (NSCF) calculation was performed to generate a spin-polarized total and projected DOS using the double k-point mesh of $16 \times 16 \times 8$ ($x = 0$) and $10 \times 10 \times 8$ ($x = 0.0625$, 0.125 and 0.25). The calculations of the dielectric tensor were carried out using density functional perturbation theory (DFPT) within random phase approximation (RPA) and independent particle approximation (IPA). Norm-conserving pseudopotentials from the SG15 database were used.

In order to predict the excitonic binding energy of all doped and pristine structures, the effective mass of the electron and hole was calculated using eqn (1) from the band structure curve. The electron effective mass and the hole effective mass were calculated from the specific band at the conduction band and valence band, respectively (depending on the optical transition of interest).

$$m^* = \hbar^2 \left[\frac{d^2E}{d^2k}\right]^{-1}. \quad (1)$$

The Wannier–Mott exciton binding energy was calculated using eqn (2),[26]

$$E_{ex} = -\frac{\mu}{m_e \varepsilon_\infty{}^2} R_y. \quad (2)$$

where $\mu = \dfrac{(m_e^* \times m_h^*)}{m_e^* + m_h^*}$ and is the reduced mass of the electron–hole pair calculated using an electron (m_e^*) and hole (m_h^*) effective mass; ε_∞ is the calculated high-frequency dielectric constant at the PBE + U level, and R_y is the Rydberg energy (13.6 eV).

The crystal structure was visualized with X-Crysden.[27] We use different supercell structures for each x of $(LaO_{1-x}F_x)MnAs$ as shown in Fig. 1. For $x = 0$, we calculate within the unit cell structure ($1 \times 1 \times 1$). Supercells $2 \times 2 \times 2$, $2 \times 2 \times 1$, and $1 \times 1 \times 2$ were used for $x = 0.0625$, 0.125, and 0.25, respectively, where F^- replaced one of the atoms at the O^{2-} site.

Results and discussions

Band structure

Fig. 2 shows the band structure of the $(LaO_{1-x}F_x)MnAs$ system with $x = 0$, 0.0625, 0.125, and 0.25, and we are only present for a single spin orientation. In Fig. 2a, the band structure for $x =$ 0 exhibits the indirect band from Γ at the valence band

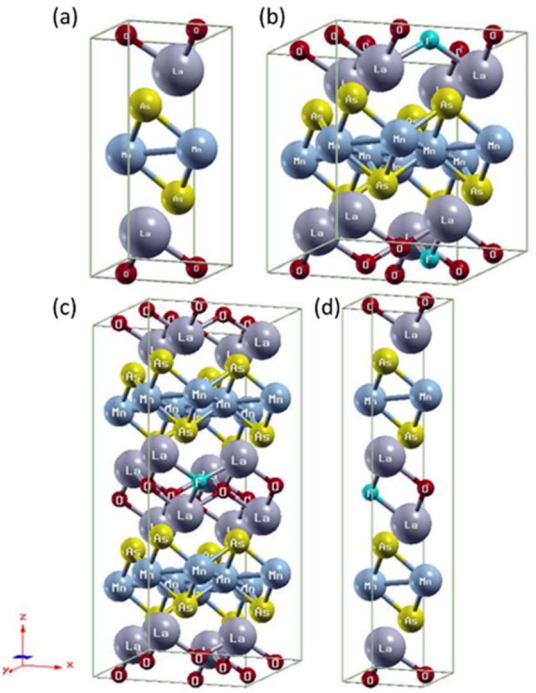

Fig. 1 Crystal structure $(LaO_{1-x}F_x)MnAs$: (a) $x = 0$, (b) $x = 0.0625$ (supercell $2 \times 2 \times 2$), (c) $x = 0.125$ (supercell $2 \times 2 \times 1$), (d) $x = 0.25$ (supercell $1 \times 1 \times 2$).

maximum (VBM) to M at the conduction band minimum (CBM) ($\Gamma \rightarrow M$) with an equal bandgap value of 0.826 eV for the spin up and spin down. This result shows not much difference from the previous calculation (0.834 eV from Γ to M) with the same U value.[21]

Increasing the x value induces a change in bandgap type to a direct bandgap, from Γ at the VBM to Γ at the CBM for $x =$ 0.0625, 0.125, 0.25, with the band gap values of 0.778 and 0.798 eV, 0.827 and 0.839 eV, and 0.488 and 0.465 eV, for spin-up and spin-down, respectively (Fig. 2b–d). Increasing the number of F doping changes the bandgap value with an irregular trend. In the higher doping concentration, we find that setting the x value to 0.0625, 0.125, and 0.25 induces the valence band to move closer to the conduction band until it passes the Fermi energy, which shows us the n-type semiconductor and metallic behavior is found and indicated by band spreading upon the Fermi level. The indirect band gap behavior at $x = 0$ shows a minimum energy transfer from Γ to M point, preferably showing in-plane electronic transport behavior. The energy transition from other high-symmetry k-points shows that the electronic transport is not completely in-plane.

Density of states

Fig. 3 shows the total DOS for the $(LaO_{1-x}F_x)MnAs$ system in the approximate range of −6 to 3 eV. Symmetrical DOS between spin-up and spin-down (Fig. 3a, d and g) are shown for $x = 0$, 0.0625, and 0.125, which indicate the antiferromagnetic properties with the local magnetic moment in the Mn site of 3.86 μ_B per Mn, 3.83 μ_B per Mn, and 3.81 μ_B per Mn, respectively. For $x = 0$, the local Mn magnetic moment is in excellent agreement with the experimental value of 3.34 μ_B at low temperatures.[28] The Mn^{2+} ion in the $[MnAs]^-$ layer contributed to this local

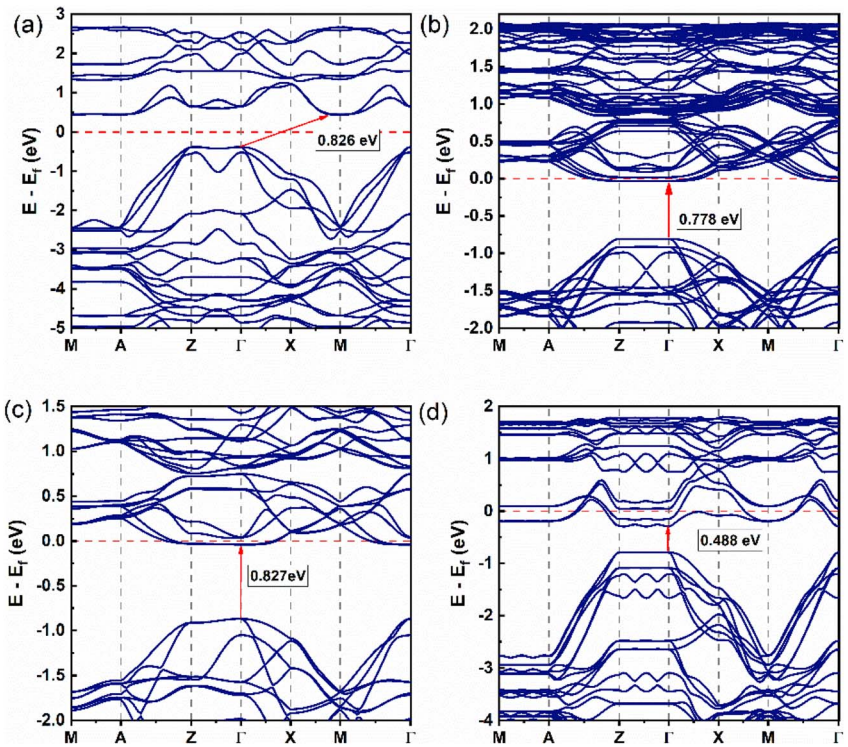

Fig. 2 Band structure of $(LaO_{1-x}F_x)MnAs$ system (single spin orientation, spin-up): (a) $x = 0$, (b) $x = 0.0625$, (c) $x = 0.125$, and (d) $x = 0.25$.

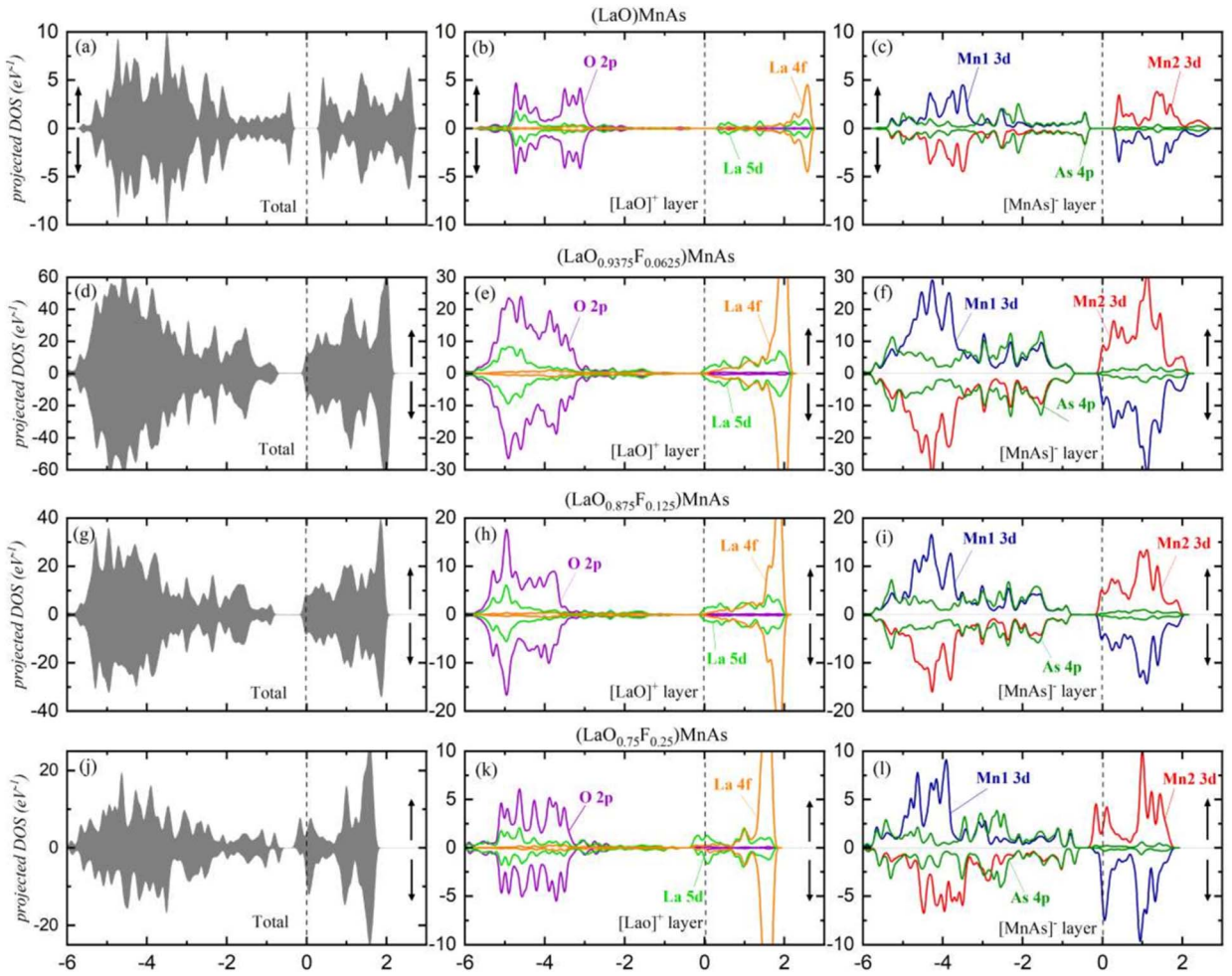

Fig. 3 (a, d, g and j) The density of states, showing the total DOS for each x value; (b, e, h and k) the projected DOS for $[LaO]^-$ layer; (c, f, i and l) the projected DOS for $[MnAs]^+$ layer.

magnetic moment.[28] Due to tetrahedral crystal field splitting, the Mn^{2+} ion can be present in a high spin ($S = 5/2$, $\mu = 5\ \mu_B$) and low spin state ($S = 1/2$, $\mu = \mu_B$). The drop in local magnetic moment can be explained by a more profound crystal field splitting, due to smaller Mn–As bond length and smaller As–Mn–As bond angles in the doped compound, which is shown in Table S1 (ESI†). Increasing x to 0.25 induces asymmetrical spin (shown in Fig. 3j), which is an indication of changes in magnetic properties. This system reveals the ferrimagnetic properties with a total magnetization of 0.78 μ_B per cell. The ferrimagnetic profile can be described using Stoner's model.[29] It states that a material would exhibit a net magnetization if $D(E_f) \times I_s \geq 1$, where $D(E_f)$ is the total density of states at the Fermi level and I_s is Stoner's parameter.[29–31] Stoner's parameter was calculated using exchange splitting Δ and the magnetization density at the Fermi level. The calculated I_s is 0.489 eV and $D(E_f)$ is 14.1 states per eV, which corresponds to $D(E_f) \times I_s = 6.91$. Our recent findings suggest that the G-type antiferromagnetic behavior of pristine (LaO)MnAs originated from the super-exchange mechanism of $MnAs_4$ tetrahedra.[21] This research suggests that the superexchange mechanism dominates in the low doping concentration, while high doping concentration (25%) is dominated by Stoner exchange-dominated ferromagnetic (FM) ordering.

To explain why high doping concentration (25%) exhibits net magnetization, we plot the pDOS of Mn d orbitals, shown in Fig. S1 (ESI†). In the pristine and lower doping concentration, the d_{yz} and d_{xz} orbitals are degenerate, as shown in the overlapping pDOS graph. In the 25% doping concentration, these orbitals' degeneracy is broken. This is due to a strong deviation in the Mn–As bond length (p and q compared to r and s, as shown in Table S1 (ESI†)), which is not exhibited in the lower doping concentration. Furthermore, there is a huge difference in Mn–As bond lengths in Mn1 and Mn2 in the 25% F-doped (LaO)MnAs. This causes different energy levels of d orbital in the Mn1 compared to Mn2 and thus gives a net magnetization. The Mn d orbital interacts with As p orbital, which is shown in Fig. S2 (ESI†), and thus the As p orbital also exhibits net magnetization.

To confirm that this net magnetization is not caused by a change in the oxidation state of Mn, as we can see from Fig. S1 (ESI†), there are still five unfilled d states above the Fermi level,

even after high doping concentration, confirming that there is no change in the Mn oxidation state. This method is also used by Hutchison *et al.* to predict the oxidation state of Fe in Fe–N–C.[32]

From the DOS graph, we found the CBM for $x = 0$ located at approximately 0.28 eV. Increasing the x value leads the CBM to move closer to the valence band (x = 0.0625, 0.125, 0.25; the CBM moving to −0.11 eV, −0.11 eV, and −0.32 eV, respectively), as also shown in the band structure. In the valence band, the highest peak was found in the approximate range of −5 to −4 eV, and in the conduction band, the highest peak was located at ∼2 eV. Different values of each DOS are caused by different cell structures (number of atoms) used for each x value.

The projected DOS are presented in Fig. 3b, e, h and k for the $[LaO]^+$ layer and in Fig. 3c, f, i and l for the $[MnAs]^-$ layer. In the layered LaO, we find that La 5d and O 2p states are deeply located in the valence band around −3 eV for all x values. With the deep separation between both states and the Fermi level (E_F), electrons in $[LaO]^+$ layers are difficult to excite to the conduction band. On the other hand, La 4f states are localized at 2.4 eV, indicating that the La 4f orbital is empty. For the approximate range from −6 to −3 eV, O 2p orbital dominates the valence band, while La 5d dominates the conduction band in the approximate range of −0.3 to 1 eV. A high peak from La 4f is shown at ∼2 eV, showing this orbital is responsible for the highest peak in the valence band that appears in the DOS. For x = 0.25, suborbital La 5d displays asymmetrical spin at ∼0.1 eV, contributing 0.169 μ_B per La to the total magnetization.

In the $[MnAs]^-$ layer, the result shows conduction bands dominated by Mn1 3d and Mn2 3d in the approximate range of −0.2 to 2 eV. In the valence band, Mn1 3d and Mn2 3d dominate the approximately −3 to 5.5 eV range, and the As 4p state spreads along with the valence band. Mn1 (red line) and Mn2 (blue line) represent opposite magnetic spin in AFM. Increasing x to 0.25 induces asymmetrical spin in Mn and As orbitals. The suborbital As 4p displays asymmetrical spin around the VBM area, which contributes 0.011 μ_B per cell to the total magnetization, and asymmetrical spin from Mn 3d contributes 0.367 μ_B per cell.

Structural parameters

Fig. 4 shows the lattice constants a and c, corresponding to the x value. F^- doping indicates a decreasing trend for a and also for c, except the c value for $x = 0.25$, which shows an increased value compared to the previous point.

The decreasing trend for a and c is probably due to different ionic radii, where F^- (1.33 Å) has a smaller ionic radius than O^{2-} (1.4 Å).[33] Thus, greater concentration of F^- induces smaller values of the lattice constant. Different trends were reported in the experiment by Naito *et al.* (2014), where they found an increasing trend of lattice constant for x = 0–0.1 (step 0.05).[16]

Optical properties

We also compare the optical properties of F-doped (LaO)MnAs and pristine (LaO)MnAs. First, we would like to discuss the

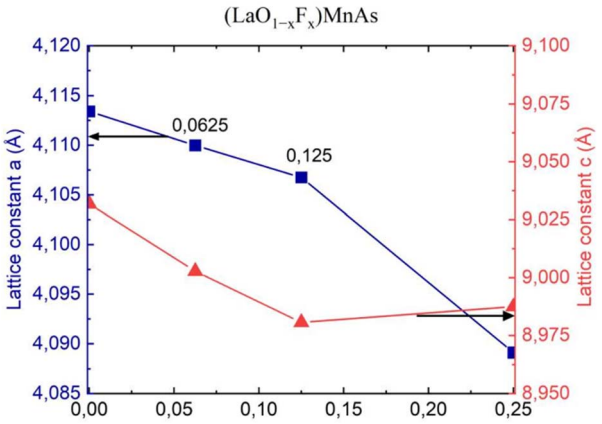

Fig. 4 Lattice constant (a, c) of $(LaO_{1-x}F_x)MnAs$ system.

calculated dielectric function of pristine (LaO)MnAs. The calculated dielectric function is shown in Fig. 6. The peaks shown in the dielectric function spectra can be assigned to its interband transition shown in Fig. 5, which is consistent with our calculated band structure. The Γ(000) and Z(001) points share the same symmetry with D_{2d} and C_{2v} point groups, respectively. These point groups are noncentrosymmetric; however, due to the nature of the centrosymmetric crystal structure of (LaO)MnAs, it allows optical transition between bands in these k-points. By using this information, we can determine the selection rules for dipolar interband transition using group theory.[34] Fig. 5 shows the proposed optical dipole interband transition near the Γ point of pristine (LaO)MnAs. As can be seen in Fig. 5, the lowest energy direct transition from VB to CB on pristine (LaO)MnAs can occur at Z–Γ–X k-points. There is a possible symmetry-allowed direct transition from the topmost valence band to the lowermost conduction band,

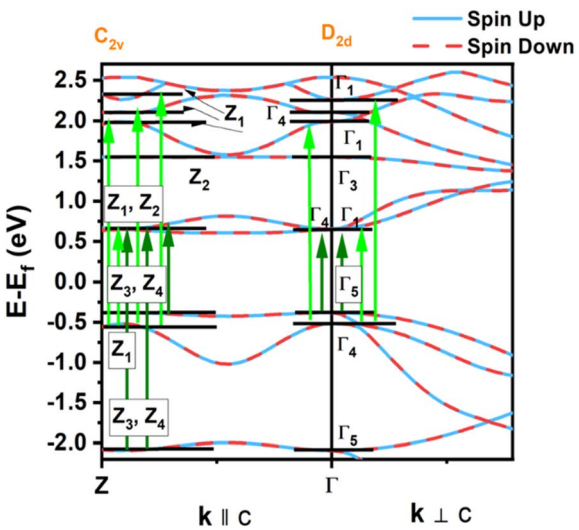

Fig. 5 Proposed optical dipole interband transition near Γ point. Light and dark green arrows represent allowed direct optical transitions in $E \| c$ and $E \perp c$, respectively. The letters assigned to every band in the special k-points are Koster notations of each symmetry species.

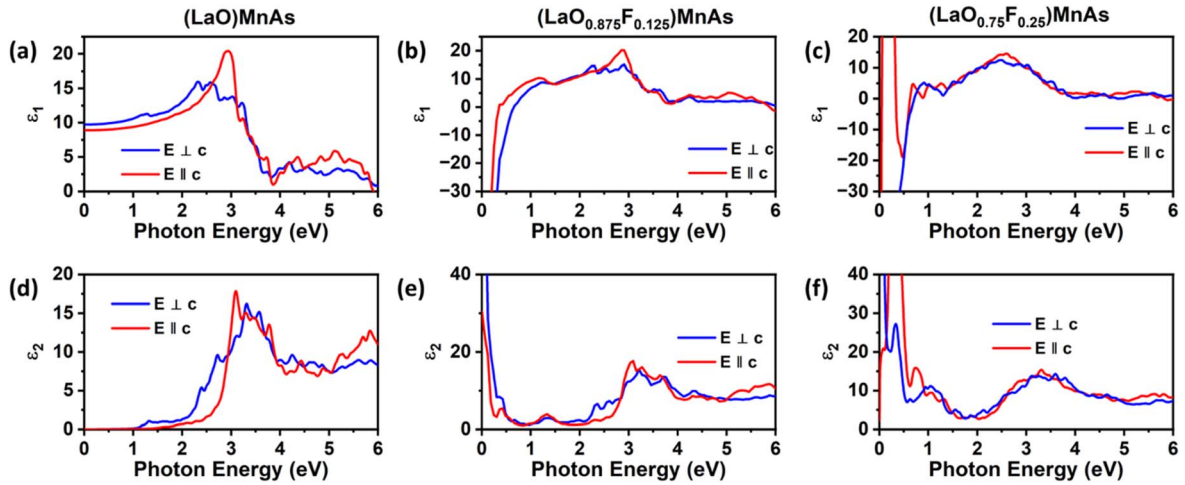

Fig. 6 Calculated real part of the dielectric function of (a) pristine (LaO)MnAs, (b) $(LaO_{0.875}F_{0.125})$MnAs, (c) $(LaO_{0.75}F_{0.25})$MnAs, and imaginary part of the dielectric function of (d) pristine (LaO)MnAs, (e) $(LaO_{0.875}F_{0.125})$MnAs, (f) $(LaO_{0.75}F_{0.25})$MnAs.

which is attributed to $\Gamma_5 \rightarrow \Gamma_4$ transition, which needs the energy of 1.0265 eV. The electron and hole effective masses on these points are $0.8952m_e$ and $1.9694m_e$. Using these values and the calculated high-frequency dielectric constant in $E \perp c$, which is $\varepsilon^{\infty} = 9.84$, gives us 86.5 meV Wannier–Mott exciton binding energy. Another low-energy direct transition is $\Gamma_5 \rightarrow \Gamma_1$ ($E_{g,da} = 1.0265$ eV, $E_b = 56$ meV) and $\Gamma_4 \rightarrow \Gamma_1$ ($E_{g,da} = 1.174$ eV, $E_b = 22$ meV), where $E_{g,da}$ and E_b are symmetry-allowed direct gap and excitonic binding energy, respectively. However, these points would not give such high excitonic binding energy as the band profile is not flat, resulting in low charge carrier effective mass. If we look at the Z point, there is a symmetry-allowed direct transition from the top of the valence band to the bottom of the conduction band, namely from $Z_3 \rightarrow Z_1$, which gives us a symmetry-allowed direct gap of 1.0178 eV. Due to the flatness of the band structure, it gives us a high $2.21m_e$ and $1.96m_e$ electron and hole effective mass, respectively corresponding to the high excitonic binding energy of 146.5 meV. This high excitonic binding energy leads us to high electron–hole interaction, which is neglected in our calculation, resulting in a blueshift compared to experimental data presented in ref. 18. A similar effect is shown in Cs_2SnI_6, which shows a comparatively similar exciton binding energy of ~130 meV, discussed in ref. 35. The imaginary part of the dielectric tensor (ε_2) is strongly related to the absorption properties of a system, which we can compare to its interband transition (Fig. 5). From Fig. 6b, we can see that ε_2 is higher if $E \perp c$ in the low-energy region; this happens because the low-energy region is dominated by $E \perp c$ symmetry-allowed transition, as illustrated in Fig. 5.

Fig. 6 shows the calculated dielectric function of pristine and doped (LaO)MnAs. The dielectric function calculation shows metallic behavior of $(LaO_{0.875}F_{0.125})$MnAs and $(LaO_{0.75}F_{0.25})$MnAs, in agreement with the electronic structure calculation. The contribution of intraband transition is shown in the low-energy region, and the higher-energy region corresponds to interband transition. The plasmon frequency of $(LaO_{0.875}F_{0.125})$MnAs is 1.88×10^{-4} cm^{-1} ($E \perp c$) and 3.45×10^{-4} cm^{-1} ($E \| c$), which can be described qualitatively using the Drude model; higher electron effective mass in $k \| c$ corresponds to a smaller frequency if $E \| c$, which can be simply seen from the band structure. These plasmonic peaks are also shown in the low-energy region in the electronic energy loss function shown in Fig. 7. Due to doping, the intraband peaks are blueshifted to the higher energy region, in line with the conclusion from electronic structure calculation that the Fermi level position shifted more to the conduction band after electron doping.

The interband transition exhibits a similar profile compared to the pristine one. Several peaks are redshifted to the lower

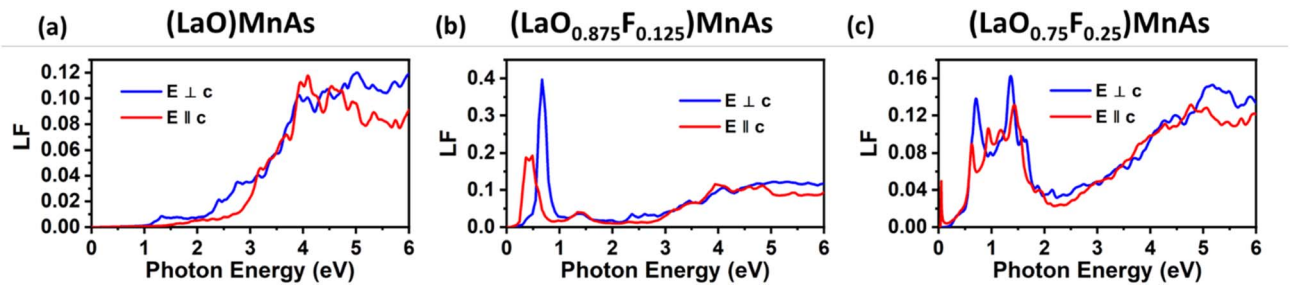

Fig. 7 Calculated electron energy loss function (LF) of (a) pristine (LaO)MnAs, (b) $(LaO_{0.875}F_{0.125})$MnAs, and (c) $(LaO_{0.75}F_{0.25})$MnAs.

energy region, which is in line with the smaller band gap conclusion from the electronic structure calculation. From the dielectric function, we can obtain its absorption coefficient, refractive index, extinction coefficient, and the optical conductivity, which shows a similar profile to its dielectric function, shown in Fig. S3 (ESI†).

To investigate the interband transition profile of the doped compound, we also calculate the momentum matrix elements (P^2) of all structures, which is shown in Fig. S4 (ESI†). Different values of P^2 occur due to the different numbers of atoms in one unit cell in every doped compound; therefore, these values cannot be compared directly.[36] The momentum matrix elements can determine the selection rule of dipolar optical transition. P^2 exhibits nearly isotropic behavior in all k-points, indicating no symmetry-forbidden transition in all k-points, enhancing its optical properties. To explain the anisotropy, take a look at several special k-points, for example, the $Z \rightarrow \Gamma$ points belonging to the C_{2v} point group and $\Gamma \rightarrow X$ points belonging to the C_s point group. In these point groups, the momentum operators in x, y, and z have different symmetry species; therefore, there is an anisotropy in these momentum matrix elements and also an anisotropy in the dielectric function curve.

Conclusions

We have studied the electronic, magnetic, and optical properties of the $(LaO_{1-x}F_x)MnAs$ system with various values of x. The results show that doping F^- ion in the O^{2-} site changes the electronic properties in terms of band structure, where the bandgap type changes from indirect to direct bandgap, accompanied by changes in E_g values. Furthermore, F doping induces changes in magnetic properties. Increasing F dopant induces decreasing local magnetic moment in the Mn site due to a more profound crystal field splitting. Increasing the x value to 0.25 changes the antiferromagnetic (AFM) to ferrimagnetic (FIM) property, with a total magnetic moment of 0.78 μ_B per cell, which is attributed mostly to Mn 3d and La 5d orbitals. The change in AFM to FIM behavior results from competition between superexchange AFM ordering and Stoner's exchange ferromagnetic ordering. In terms of lattice constant, F doping induces a decreasing trend for a and c. Pristine (LaO)MnAs exhibited a high excitonic binding energy (~146 meV) due to a flat band profile at the VBM and CBM. There is no symmetry-forbidden direct transition from VB to CB in every k-point in both pristine and doped compounds, which enhances its optical properties. Doped (LaO)MnAs exhibits metallic behavior in both optical and electronic properties.

Author contributions

Jessie Manopo: methodology, investigation, visualization, formal analysis, writing – original draft. Tio Prince Lubis: investigation, visualization, formal analysis, writing – review and editing. Muhammad Arief Mustajab Enha Maryono: writing – review and editing. Pepen Arifin: writing – review and editing. Toto Winata: writing – review and editing. Rena Widita: formal analysis, validation, writing – review and editing. Yudi Darma: conceptualization, validation, writing – review and editing, supervision, project administration.

Conflicts of interest

There are no conflicts to declare.

Acknowledgements

This work is partly supported by the Ministry of Education, Culture, Research and Technology of the Republic of Indonesia through the 2022–2023 research program, Riset Unggulan and PPMI from the ITB research program year 2023. J. M. acknowledges Pendidikan Magister menuju Doktor untuk Sarjana Unggul (PMDSU) batch VI scholarship from the Ministry of Education, Culture, Research and Technology of the Republic of Indonesia. The calculation was partially performed at the High Performance Computing (HPC) facility provided by the Research Centre for Nanoscience and Nanotechnology, Institut Teknologi Bandung (ITB), and the HPC facility provided by the Department of Physics, ITB. The authors also thank S. Muhammady for the discussion and technical assistance.

Notes and references

1 Y. Kamihara, T. Watanabe, M. Hirano and H. Hosono, *J. Am. Chem. Soc.*, 2008, **130**, 3296–3297.
2 H. Yanagi, R. Kawamura, T. Kamiya, Y. Kamihara, M. Hirano, T. Nakamura, H. Osawa and H. Hosono, *Phys. Rev. B: Condens. Matter Mater. Phys.*, 2008, **77**, 224431.
3 H. Ohta and K. Yoshimura, *Phys. Rev. B: Condens. Matter Mater. Phys.*, 2009, **80**, 184409.
4 Y. K. Li, X. F. Xu, C. Cao, C. Y. Shen, Y. K. Luo, Q. Tao, X. Lin, L. Zhang, G. H. Cao and Z. A. Xu, *Phys. Rev. B: Condens. Matter Mater. Phys.*, 2012, **86**, 104408.
5 T. Watanabe, H. Yanagi, Y. Kamihara, T. Kamiya, M. Hirano and H. Hosono, *J. Solid State Chem.*, 2008, **181**, 2117–2120.
6 Z. Li, G. Chen, J. Dong, G. Li, W. Hu, D. Wu, S. Su, P. Zheng, T. Xiang, N. Wang and J. Luo, *Phys. Rev. B: Condens. Matter Mater. Phys.*, 2008, **78**, 060504.
7 S. Komatsuzaki, Y. Ohki, M. Sasaki, Y. Takahashi, K. Takase, Y. Takano and K. Sekizawa, *AIP Conf. Proc.*, 2006, **850**, 1255–1256.
8 K. Kayanuma, H. Hiramatsu, M. Hirano, R. Kawamura, H. Yanagi, T. Kamiya and H. Hosono, *Phys. Rev. B: Condens. Matter Mater. Phys.*, 2007, **76**, 195325.
9 K. Kayanuma, R. Kawamura, H. Hiramatsu, H. Yanagi, M. Hirano, T. Kamiya and H. Hosono, *Thin Solid Films*, 2008, **516**, 5800–5804.
10 S. Muhammady, A. S. Erlyanti, R. Widita and Y. Darma, *Int. J. Quantum Chem.*, 2020, **120**, e26090.
11 N. Emery, E. J. Wildman, J. M. S. Skakle, G. Giriat, R. I. Smith and A. C. McLaughlin, *Chem. Commun.*, 2010, **46**, 6777–6779.
12 K. Takase, S. Hiramoto, T. Fukushima, K. Sato, C. Moriyoshi and Y. Kuroiwa, *Appl. Phys. Express*, 2017, **10**, 123001.

13 A. P. Wijnheijmer, X. Martí, V. Holý, M. Cukr, V. Novák, T. Jungwirth and P. M. Koenraad, *Appl. Phys. Lett.*, 2012, **100**, 112107.
14 T. Jungwirth, V. Novák, X. Martí, M. Cukr, F. Máca, A. B. Shick, J. Mašek, P. Horodyská, P. Němec, V. Holý, J. Zemek, P. Kužel, I. Němec, B. L. Gallagher, R. P. Campion, C. T. Foxon and J. Wunderlich, *Phys. Rev. B: Condens. Matter Mater. Phys.*, 2011, **83**, 035321.
15 M. Zingl, E. Assmann, P. Seth, I. Krivenko and M. Aichhorn, *Phys. Rev. B*, 2016, **94**, 045130.
16 A. Naito, Y. Morosawa, T. Watanabe, Y. Takano and K. Takase, in *Proceedings of the 12th Asia Pacific Physics Conference (APPC12)*, Journal of the Physical Society of Japan, 2014, vol. 1.
17 K. Kayanuma, H. Hiramatsu, T. Kamiya, M. Hirano and H. Hosono, *J. Appl. Phys.*, 2009, **105**, 073903.
18 A. Beleanu, J. Kiss, G. Kreiner, C. Köhler, L. Müchler, W. Schnelle, U. Burkhardt, S. Chadov, S. Medvediev, D. Ebke, C. Felser, G. Cordier, B. Albert, A. Hoser, F. Bernardi, T. I. Larkin, D. Pröpper, A. V. Boris and B. Keimer, *Phys. Rev. B: Condens. Matter Mater. Phys.*, 2013, **88**, 184429.
19 A. Higashiya, K. Nakagawa, A. Yamasaki, K. Nagai, S. Fujioka, Y. Kanai, K. Yamagami, H. Fujiwara, A. Sekiyama, A. Abozeed, T. Kadono, S. Imada, K. Kuga, M. Yabashi, K. Tamasaku, T. Ishikawa, S. Toyama and K. Takase, *J. Electron Spectrosc. Relat. Phenom.*, 2017, **220**, 58–60.
20 K. Takase, A. Naito, A. Higashiya, T. Kadono and S. Imada, *Phys. Procedia*, 2015, **75**, 455–459.
21 R. Widita, S. Muhammady, R. D. Prasetiyawati, R. Marlina, L. Suryanegara, B. Purnama, R. Kurniadi and Y. Darma, *ACS Omega*, 2021, **6**, 4440–4447.
22 P. Giannozzi, S. Baroni, N. Bonini, M. Calandra, R. Car, C. Cavazzoni, D. Ceresoli, G. L. Chiarotti, M. Cococcioni, I. Dabo, A. Dal Corso, S. De Gironcoli, S. Fabris, G. Fratesi, R. Gebauer, U. Gerstmann, C. Gougoussis, A. Kokalj, M. Lazzeri, L. Martin-Samos, N. Marzari, F. Mauri, R. Mazzarello, S. Paolini, A. Pasquarello, L. Paulatto, C. Sbraccia, S. Scandolo, G. Sclauzero, A. P. Seitsonen, A. Smogunov, P. Umari and R. M. Wentzcovitch, *J. Phys.: Condens. Matter*, 2009, **21**, 395502.
23 S. Muhammady, Y. Kurniawan, M. A. K. Purbayanto and Y. Darma, *Mater. Res. Express*, 2018, **5**, 066303.
24 J. P. Perdew, K. Burke and M. Ernzerhof, *Phys. Rev. Lett.*, 1996, **77**, 3865–3868.
25 J. Hubbard, *Proc. R. Soc. London, Ser. A*, 1963, **276**, 238–257.
26 M. A. Fox, *Optical Properties of Solids, Oxford Master Series in Physics*, Oxford University Press, Oxford, 2002.
27 A. Kokalj, *Comput. Mater. Sci.*, 2003, **28**, 155–168.
28 N. Emery, E. J. Wildman, J. M. S. Skakle, A. C. McLaughlin, R. I. Smith and A. N. Fitch, *Phys. Rev. B: Condens. Matter Mater. Phys.*, 2011, **83**, 144429.
29 P. M. Marcus and V. L. Moruzzi, *Phys. Rev. B: Condens. Matter Mater. Phys.*, 1988, **38**, 6949.
30 G. M. Dalpian, J. L. F. Da Silva and S. H. Wei, *Phys. Rev. B: Condens. Matter Mater. Phys.*, 2009, **79**, 241201.
31 M. Mi, X. Zheng, S. Wang, Y. Zhou, L. Yu, H. Xiao, H. Song, B. Shen, F. Li, L. Bai, Y. Chen, S. Wang, X. Liu and Y. Wang, *Adv. Funct. Mater.*, 2022, **32**, 2112750.
32 P. Hutchison, P. S. Rice, R. E. Warburton, S. Raugei and S. Hammes-Schiffer, *J. Am. Chem. Soc.*, 2022, **144**, 16524–16534.
33 R. D. Shannon, *Acta Crystallogr., Sect. A: Cryst. Phys., Diffr., Theor. Gen. Crystallogr.*, 1976, **32**, 751–767.
34 M. S. Dresselhaus, G. Dresselhaus and A. Jorio, *Group theory*, Springer Berlin Heidelberg, 2008.
35 S. R. Kavanagh, C. N. Savory, S. M. Liga, G. Konstantatos, A. Walsh and D. O. Scanlon, *J. Phys. Chem. Lett.*, 2022, **13**, 10965–10975.
36 W. Meng, X. Wang, Z. Xiao, J. Wang, D. B. Mitzi and Y. Yan, *J. Phys. Chem. Lett.*, 2017, **8**, 2999–3007.